

Large-scale circulations in a shear-free convective turbulence: Mean-field simulations

Cite as: Phys. Fluids **34**, 105121 (2022); <https://doi.org/10.1063/5.0110716>

Submitted: 16 July 2022 • Accepted: 14 September 2022 • Accepted Manuscript Online: 16 September 2022 • Published Online: 14 October 2022

G. Orian, A. Asulin, E. Tkachenko, et al.



View Online



Export Citation



CrossMark

ARTICLES YOU MAY BE INTERESTED IN

[The bimodal instability of thermal convection in a tall vertical annulus](#)

Physics of Fluids **34**, 104102 (2022); <https://doi.org/10.1063/5.0105030>

[A hybrid Cartesian-meshless method for the simulation of thermal flows with complex immersed objects](#)

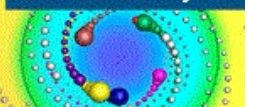
Physics of Fluids (2022); <https://doi.org/10.1063/5.0100224>

[Review of Coating and Curing Processes: Evaluation in Automotive Industry](#)

Physics of Fluids (2022); <https://doi.org/10.1063/5.0109376>

Physics of Fluids
Special Topic: Cavitation

Submit Today!



Large-scale circulations in a shear-free convective turbulence: Mean-field simulations

Cite as: Phys. Fluids **34**, 105121 (2022); doi: 10.1063/5.0110716

Submitted: 16 July 2022 · Accepted: 14 September 2022 ·

Published Online: 14 October 2022



View Online



Export Citation



CrossMark

G. Orian,^{1,2} A. Asulin,¹ E. Tkachenko,¹ N. Kleeorin,¹  A. Levy,¹  and I. Rogachevskii^{1,a)} 

AFFILIATIONS

¹The Pearlstone Center for Aeronautical Engineering Studies, Department of Mechanical Engineering, Ben-Gurion University of the Negev, P.O. Box 653, Beer-Sheva 84105, Israel

²Nuclear Research Center, Negev P.O. Box 9001, Beer-Sheva 84190, Israel

^{a)} Author to whom correspondence should be addressed: gary@bgu.ac.il

ABSTRACT

It has been previously shown [Elperin *et al.*, “Formation of large-scale semi-organized structures in turbulent convection,” Phys. Rev. E **66**, 066305 (2002)] that a non-rotating turbulent convection with nonuniform large-scale flows contributes to the turbulent heat flux. As a result, the turbulent heat flux depends explicitly not only on the gradients of the large-scale temperature, but also on the gradients of the large-scale velocity. This is because the nonuniform large-scale flows produce anisotropic velocity fluctuations, which modify the turbulent heat flux. This effect causes an excitation of a convective-wind instability and formation of large-scale semi-organized coherent structures (large-scale convective cells). In the present study, we perform mean-field numerical simulations of shear-free convection, which take into account the modification of the turbulent heat flux by nonuniform large-scale flows. We use periodic boundary conditions in horizontal direction as well as stress-free or no-slip boundary conditions in vertical direction. We show that the redistribution of the turbulent heat flux by the nonuniform large-scale motions in turbulent convection plays a crucial role in the formation of the large-scale semi-organized coherent structures. In particular, this effect results in a strong reduction of the critical effective Rayleigh number (based on the eddy viscosity and turbulent temperature diffusivity) required for the formation of the large-scale convective cells. We demonstrate that the convective-wind instability is excited when the scale separation ratio between the height of the convective layer and the integral turbulence scale is large. The level of the mean kinetic energy at saturation increases with the scale separation ratio. We also show that inside the large-scale convective cells, there are local regions with the positive vertical gradient of the potential temperature, which implies that these regions are stably stratified.

© 2022 Author(s). All article content, except where otherwise noted, is licensed under a Creative Commons Attribution (CC BY) license (<http://creativecommons.org/licenses/by/4.0/>). <https://doi.org/10.1063/5.0110716>

I. INTRODUCTION

Turbulent non-rotating convection has been investigated in theoretical studies,^{1–8} laboratory experiments,^{4,5,9–26} numerical simulations,^{27–36} and atmospheric observations.^{37–41} One of the key features of turbulent convection is the formation of coherent semi-organized structures, referred to as large-scale convective cells (or large-scale circulations) in a shear-free convection and large-scale rolls in a sheared convection. Spatial scales of the large-scale coherent structures in a turbulent convection are much larger than turbulent scales, and their lifetime is much longer than the characteristic turbulent timescale.

Buoyancy-driven structures, such as plumes, jets, and large-scale circulation patterns are observed in numerous laboratory experiments on turbulent convection. The large-scale circulations caused by convection in the Rayleigh–Bénard apparatus are often called the “mean wind.”¹¹ There are several open questions concerning these flows, e.g., how do they arise, and what are their characteristics and dynamics.

In atmospheric turbulent convection, two types of coherent semi-organized structures, namely, “cloud cells” in a shear-free convection and “cloud streets,” in a sheared convection have been observed.^{38,39,41} In particular, cloud cells are seen as three-dimensional, long-lived Bénard-type cells consisting in narrow uprising plumes and wide down-draughts. These structures occupy the entire convective boundary layer of about 1–3 km in height. In the sheared convective boundary layer with a strong wind, the cloud streets are seen as large-scale rolls stretched along the wind.

In spite of a number of theoretical and numerical studies, the nature of large-scale coherent structures in turbulent convection is a subject of active discussions. There are two points of view on the origin of large-scale circulation in turbulent convection. According to one point of view, the large-scale circulations which develop at low Rayleigh numbers near the onset of convection continually increase their size as the Rayleigh numbers is increased and continue to exist in

an average sense at even very high Rayleigh numbers.²⁷ Another hypothesis holds that the large-scale circulation is a genuine high Rayleigh number effect.¹¹

A mean-field theory of non-rotating turbulent convection has been developed in Refs. 42 and 43, where the convective-wind instability in the shear-free turbulent convection causing the formation of large-scale cells is identified. In the sheared turbulent convection, the convective-shear instability resulting in formation of large-scale rolls can be excited.^{42,43} A redistribution of the turbulent heat flux by non-uniform large-scale motions plays a crucial role in the formation of the large-scale coherent structures in turbulent convection. To determine key parameters that affect formation of the large-scale coherent structures in the turbulent convection, the linear stage of the convective-wind and convective-shear instabilities has been numerically studied in Ref. 44.

In the present study we perform mean-field numerical simulations to study nonlinear evolution of large-scale circulations in turbulent shear-free convection taking into account the effect of modification of the turbulent heat flux by non-uniform large-scale motions. This paper is organized as follows. In Sec. II, we discuss a modification of the turbulent heat flux caused by anisotropic velocity fluctuations in turbulence with non-uniform large-scale flows. In Sec. III, we formulate the non-dimensional equations, the governing non-dimensional parameters and discuss the large-scale convective-wind instability. In Sec. IV, we describe the set-up for the mean-field numerical simulations and discuss the results of the numerical simulations for periodic boundary conditions in horizontal direction as well as stress-free or no-slip boundary conditions in vertical direction. In Sec. V, we discuss the novelty aspects and significance of the obtained results as well as their applications. Finally, conclusions are drawn in Sec. VI.

II. TURBULENT CONVECTION AND TURBULENT HEAT FLUX

We consider turbulent convection with very high Rayleigh numbers, and large Reynolds and Peclet numbers. Formation of coherent semi-organized structures is usually studied using a mean field approach whereby the velocity \mathbf{U} , pressure P , and potential temperature Θ are decomposed into the mean and fluctuating parts: $\mathbf{U} = \bar{\mathbf{U}} + \mathbf{u}$, $P = \bar{P} + p$, and $\Theta = \bar{\Theta} + \theta$, the fluctuating parts have zero mean values, which implies the Reynolds averaging. Here $\bar{\mathbf{U}} = \langle \mathbf{U} \rangle$ is the mean velocity, $\bar{P} = \langle P \rangle$ is the mean pressure and $\bar{\Theta} = \langle \Theta \rangle$ is the mean potential temperature, and \mathbf{u} , p , and θ are fluctuations of velocity, pressure and potential temperature, respectively. Averaging the Navier–Stokes equation and equation for the potential temperature over an ensemble, we obtain the mean-field equations,

$$\left(\frac{\partial}{\partial t} + \bar{\mathbf{U}} \cdot \nabla\right) \bar{U}_i = -\nabla_i \left(\frac{\bar{P}}{\bar{\rho}_0}\right) - \nabla_j \langle u_i u_j \rangle + \beta \bar{\Theta} e_i, \quad (1)$$

$$\left(\frac{\partial}{\partial t} + \bar{\mathbf{U}} \cdot \nabla\right) \bar{\Theta} = -(\bar{\mathbf{U}} \cdot \nabla) \bar{T}_0 - \nabla_i \langle u_i \theta \rangle, \quad (2)$$

and $\text{div } \bar{\mathbf{U}} = 0$, where the mean potential temperature $\bar{\Theta}$ is related to the physical temperature \bar{T} as: $\bar{\Theta} = \bar{T} (\bar{P}_0/\bar{P})^{1-1/\gamma}$, where \bar{T} is the mean physical temperature and \bar{T}_0 is the mean physical temperature in the equilibrium (the basic reference state), \bar{P} is the mean pressure and \bar{P}_0 is the mean pressure in the equilibrium, $\bar{\rho}_0$ is the mean fluid

density in the equilibrium, $\gamma = c_p/c_v$ is the specific heats ratio, $\beta = g/\bar{T}_0$ is the buoyancy parameter, \mathbf{g} is the gravity acceleration, and $\bar{\rho}_0$ is the mean fluid density. Equations (1) and (2) are written in the Boussinesq approximation with $\text{div } \bar{\mathbf{U}} = 0$.

In Eqs. (1) and (2), we neglect very small terms caused by kinematic viscosity and molecular diffusivity of temperature in comparison with the terms due to turbulent viscosity and turbulent diffusivity. The mean velocity $\bar{\mathbf{U}}(t, \mathbf{x})$, the mean potential temperature $\bar{\Theta}(t, \mathbf{x})$, and the mean pressure $\bar{P}(t, \mathbf{x})$ in Eqs. (1) and (2) describe deviations from the hydrostatic equilibrium without mean motions: $\nabla \bar{P}_0 = \bar{\rho}_0 \mathbf{g}$ and $\bar{\rho}_0 = \text{const}$, where $\mathbf{g} = -g \mathbf{e}$ and \mathbf{e} is the vertical unit vector.

The effect of convective turbulence on the mean velocity and mean potential temperature is described by the Reynolds stress $\langle u_i u_j \rangle$ and turbulent flux of potential temperature $\mathbf{F} = \langle \mathbf{u}\theta \rangle$. Traditional theoretical turbulence models, such as the Kolmogorov-type local closures, imply that the turbulent flux of momentum determined by $\langle u_i u_j \rangle$ and the turbulent flux of potential temperature \mathbf{F} are assumed to be proportional to the local mean gradients, whereas the proportionality coefficients, namely, turbulent viscosity and turbulent temperature diffusivity, are uniquely determined by local turbulent parameters. The classical expression for the Reynolds stress is $\langle u_i u_j \rangle = -\nu_T (\nabla_i \bar{U}_j + \nabla_j \bar{U}_i)$ and the classical turbulent heat flux is given by $\mathbf{F} = -\kappa_T \nabla \bar{\Theta}$ (see, e.g., Ref. 7), where ν_T is the turbulent viscosity and κ_T is the turbulent temperature diffusivity.

On the other hand, there are coherent structures in turbulent convection (large-scale coherent convective cells or large-scale circulations) and the velocity field inside large-scale circulations is strongly nonuniform. These nonuniform motions can produce anisotropic velocity fluctuations which can contribute to the turbulent heat flux. In particular, the turbulent heat flux, $\mathbf{F} = -\kappa_T \nabla \bar{\Theta}$, does not take into account the contribution from anisotropic velocity fluctuations.

It has been shown in Ref. 42 that the contribution to the turbulent heat flux from anisotropic velocity fluctuations plays essential role in formation of large-scale circulations in turbulent convection. In particular, the following expression for the turbulent heat flux \mathbf{F} has been derived in Ref. 42:

$$\mathbf{F} = \mathbf{F}^* - \tau_0 \left[\mathbf{F}_z^* \text{div } \bar{\mathbf{U}}_{\perp} - \frac{1}{2} \bar{\mathbf{W}} \times \mathbf{F}_z^* \right], \quad (3)$$

where $\mathbf{F}^* = -\kappa_T \nabla \bar{\Theta}$ is the classical turbulent heat flux (i.e., the background turbulent heat flux in the absence of nonuniform large-scale flows), τ_0 is the correlation time of turbulent velocity at the integral scale of turbulent motions, $\bar{\mathbf{W}} = \nabla \times \bar{\mathbf{U}}$ is the mean vorticity, the mean velocity $\bar{\mathbf{U}} = \bar{\mathbf{U}}_{\perp} + \bar{U}_z \mathbf{e}$ is decomposed into the horizontal $\bar{\mathbf{U}}_{\perp}$ and vertical \bar{U}_z components. The new terms in the turbulent heat flux \mathbf{F} are caused by anisotropic velocity fluctuations and depend on the mean velocity gradients. These new terms lead to the excitation of large-scale convective-wind instability and formation of coherent structures. For nearly uniform large-scale flows, the anisotropic turbulence effects can be neglected, so that the traditional equation for the turbulent heat flux is recovered.

The physical meaning of the new terms in the turbulent heat flux is the following. The first term $\mathbf{F}_{\text{new}} = -\tau_0 \mathbf{F}_z^* \text{div } \bar{\mathbf{U}}_{\perp}$ in the squared brackets of Eq. (3) for the turbulent heat flux describes the redistribution of the vertical background turbulent heat flux \mathbf{F}_z^* by the perturbations of the convergent (or divergent) horizontal mean flows $\bar{\mathbf{U}}_{\perp}$ (see Fig. 1). This redistribution of the vertical turbulent heat flux occurs

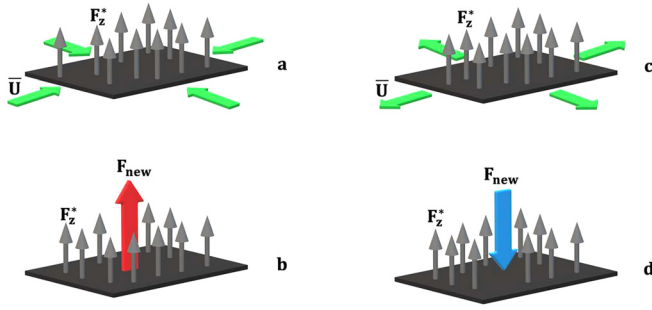


FIG. 1. The illustration of the physics caused by the new turbulent heat flux $F_{\text{new}} = -\tau_0 F_z^* \text{div } \bar{U}_\perp$ produced by the perturbations of the convergent (or divergent) horizontal mean flows \bar{U}_\perp [shown by the green arrows in panels (a) and (c)]. The new turbulent flux F_{new} increases the upward (positive) heat flux, enhances buoyancy, and increases the local mean potential temperature, thus creating the upward flow. Likewise, the new turbulent flux F_{new} decreases the vertical turbulent flux of potential temperature by the divergent horizontal motions, which reduces the buoyancy and decreases the local mean potential temperature, thus creating the downward flow. These effects cause a formation of the large-scale coherent structures (the large-scale circulations).

during the lifetime of turbulent eddies. In particular, the term F_{new} describes enhancing of the vertical turbulent flux of potential temperature by the converging horizontal motions. The latter increases the upward (positive) heat flux and enhances buoyancy, thus creating the upward flow. In its turn, this flow strengthens the horizontal convergent flow causing a large-scale convective-wind instability.

The second term $\propto (\tau_0/2) (\bar{W} \times F_z^*)$ in the squared brackets of Eq. (3) determines the formation of the horizontal turbulent heat flux due to “rotation” of the vertical background turbulent heat flux F_z^* by the perturbations of the horizontal mean vorticity \bar{W}_\perp . In particular, this term describes generation of horizontal turbulent flux of potential temperature through turning the vertical flux by horizontal component of the vorticity. This effect decreases (increases) local potential temperatures in rising motions, that reduces the buoyancy accelerations, and weakens vertical velocity and vorticity, and thus causes damping of large-scale convective-wind instability. These two effects are determined by the local inertial forces in nonuniform mean flows.

The linear-stability analysis of the linearized Eqs. (1)–(3) yields the following estimate for the growth rate $\tilde{\gamma}_{\text{inst}}$ of long-wave perturbations [$(\ell_0 K)^2 \ll 1$] of the convective-wind instability:

$$\tilde{\gamma}_{\text{inst}} = \left(\frac{\beta F_z^* \tau_0}{2} \right)^{1/2} K |\sin \varphi| (1 - 2 \sin^2 \varphi)^{1/2} - \nu_T K^2, \quad (4)$$

where φ is the angle between the vertical axis z and the wave vector \mathbf{K} of small perturbations and u_0 is the characteristic turbulent velocity in the integral scale ℓ_0 of turbulence. Equation (4) is obtained for the turbulent Prandtl number $\text{Pr}_T = 1$. The analysis of the convective-wind instability is performed in Refs. 42–44. The mechanism of this instability is as follows (see Fig. 1). When $\nabla_z \bar{U}_z > 0$, perturbations of the vertical velocity \tilde{U}_z cause negative divergence of the horizontal velocity, $\text{div } \bar{U}_\perp < 0$ (provided that $\text{div } \bar{U} = 0$), describing convergent horizontal flows (shown by the green arrows in panel a of Fig. 1). This produces vertical turbulent flux of potential temperature $F_{\text{new}} = -\tau_0 F_z^* \text{div } \bar{U}_\perp$ (shown by the red arrow in panel b of Fig. 1). The latter strengthens the local vertical turbulent flux of potential temperature and by this

means leads to increasing the local mean potential temperature and buoyancy. The latter enhances the local mean vertical velocity \bar{U}_z . Through this mechanism, a large-scale convective-wind instability is excited.

Similar reasoning is valid when $\nabla_z \bar{U}_z < 0$, whereas $\text{div } \bar{U}_\perp > 0$ describing divergent horizontal flows (shown by the green arrows in panel c of Fig. 1). This produces negative perturbations of the vertical flux of potential temperature $F_{\text{new}} = -\tau_0 F_z^* \text{div } \bar{U}_\perp$ (shown by the blue arrow in panel d of Fig. 1), which lead to decrease in the mean potential temperature and buoyancy. This enhances the downward flow, and results in excitation of the convective-wind instability. Thus, nonzero perturbations of $\text{div } \bar{U}_\perp$ cause redistribution of the vertical turbulent flux of potential temperature and formation of regions with large values of this flux. The regions where $\nabla_z \bar{U}_z < 0$ alternate with the low-flux regions where $\nabla_z \bar{U}_z > 0$. This mechanism causes formation of the large-scale circulations.

III. NONDIMENSIONAL EQS. AND LARGE-SCALE CONVECTIVE-WIND INSTABILITY

Using the expression (3) for the turbulent heat flux F with the additional terms caused by the nonuniform mean flows, calculating $\text{div } F$, and assuming that the nondimensional total vertical heat flux $\Phi_c = \tilde{F}_z^* + \tilde{U}_z \tilde{\Theta}$ is constant, we rewrite Eqs. (1) and (2) in a nondimensional form,

$$\frac{\partial \tilde{U}}{\partial t} + (\tilde{U} \cdot \nabla) \tilde{U} = -\frac{\nabla \tilde{P}}{\rho_0} + \text{Ra}_T \tilde{\Theta} \mathbf{e} + \Delta \tilde{U}, \quad (5)$$

$$\begin{aligned} \text{Pr}_T \left(\frac{\partial \tilde{\Theta}}{\partial t} + (\tilde{U} \cdot \nabla) \tilde{\Theta} \right) &= \tilde{U}_z + \Delta \tilde{\Theta} + \epsilon \left[(\nabla_z \tilde{U}_z) \times \nabla_z (\tilde{U}_z \tilde{\Theta}) \right. \\ &+ (\Phi_c - \tilde{U}_z \tilde{\Theta}) \left(\frac{\Delta}{2} - \nabla_z^2 \right) \tilde{U}_z \\ &+ \frac{1}{2} (\nabla_z \tilde{U}_x - \nabla_x \tilde{U}_z) \nabla_x (\tilde{U}_z \tilde{\Theta}) \\ &\left. + \frac{1}{2} (\nabla_z \tilde{U}_y - \nabla_y \tilde{U}_z) \nabla_y (\tilde{U}_z \tilde{\Theta}) \right], \quad (6) \end{aligned}$$

and $\text{div } \tilde{U} = 0$ (see Appendix A), where \tilde{U} is the nondimensional mean velocity, \tilde{F}_z^* is the nondimensional vertical turbulent background heat flux, $\tilde{\Theta}$ is the nondimensional mean potential temperature and \tilde{P} is the nondimensional mean pressure, and \mathbf{e} is the unit vector directed along the vertical z axis.

In Eqs. (5) and (6), length is measured in the units of the vertical size of the convective layer L_z (e.g., the size of the computational domain), time is measured in the units of the turbulent viscosity time, L_z^2/ν_T , velocity is measured in the units of ν_T/L_z , potential temperature is measured in the units of $L_z N^2 \text{Pr}_T/\beta$, turbulent heat flux is measured in the units of $\nu_T N^2 \text{Pr}_T/\beta$, and pressure is measured in the units of $\rho_0 (\nu_T/L_z)^2$. Here, $\nu_T = u_0 \ell_0/3$ is the turbulent (eddy) viscosity, u_0 is the turbulent velocity at the integral turbulent scale ℓ_0 , and $N^2 = \beta |\nabla_z \bar{T}_0|$.

In Eqs. (5) and (6), we use the following dimensionless parameters:

- the effective Rayleigh number,

$$Ra_T = \frac{L_z^4 N^2}{\nu_T \kappa_T}, \tag{7}$$

- the turbulent Prandtl number,

$$Pr_T = \frac{\nu_T}{\kappa_T}, \tag{8}$$

- the scale separation parameter,

$$\epsilon = \frac{\ell_0^2}{3L_z^2}, \tag{9}$$

- the non-dimensional total vertical heat flux,

$$\Phi_c = \frac{3}{\epsilon^2 Ra_T} \left(\frac{u_c}{u_0} \right)^3 = \frac{\sigma}{\epsilon^2 Ra_T}, \tag{10}$$

where $\sigma = 3(u_c/u_0)^3$, $u_c = (\beta F_z^* \ell_0)^{1/3}$ is the characteristic turbulent convective velocity, F_z^* is the vertical background turbulent flux of potential temperature and κ_T is the turbulent (eddy) diffusivity. In Eqs. (5) and (6), we have neglected small terms $\sim O(\epsilon^2)$, where $\epsilon \ll 1$.

Let us discuss the large-scale convective-wind instability, using the stress-free boundary conditions for the velocity field in the vertical direction (along the z axis),

$$\tilde{U}_z(t, z = 0) = \tilde{U}_z(t, z = 1) = 0, \tag{11}$$

$$\nabla_z \tilde{U}_x(t, z = 0) = \nabla_z \tilde{U}_x(t, z = 1) = 0, \tag{12}$$

$$\nabla_z \tilde{U}_y(t, z = 0) = \nabla_z \tilde{U}_y(t, z = 1) = 0. \tag{13}$$

For a classical laminar convection with the boundary conditions given by Eqs. (11)–(13), the critical Rayleigh number required for the onset of convection is $Ra_{cr} \approx 657.5$.^{44–47} The classical laminar convection is described by Eqs. (5) and (6), where there are no terms $\propto \epsilon$ in Eq. (6), and turbulent viscosity and turbulent heat conductivity are replaced by the molecular viscosity and heat conductivity.

Now let us consider the linear two-dimensional problem using Eqs. (5) and (6) with $\epsilon \neq 0$, where we take into account the modification of the turbulent heat flux by nonuniform large-scale motions. A particular solution of the linearized Eqs. (5) and (6), satisfying the vertical boundary conditions (11)–(13), is given by

$$\tilde{U}_z(t, y, z) = U_0 \sin(\pi z) \cos(\alpha \pi y) \exp(\gamma_{inst} t), \tag{14}$$

$$\tilde{U}_y(t, y, z) = -\alpha^{-1} U_0 \cos(\pi z) \sin(\alpha \pi y) \exp(\gamma_{inst} t), \tag{15}$$

$$\tilde{\Theta}(t, y, z) = \Theta_0 \sin(\pi z) \cos(\alpha \pi y) \exp(\gamma_{inst} t), \tag{16}$$

and $\tilde{U}_x(t, y, z) = 0$, where γ_{inst} is the non-dimensional growth rate of the convective-wind instability, and the parameter α to be determined below. Equations (14)–(16) imply that the nondimensional wavenumbers $K_y = \alpha\pi$ and $K_z = \pi$, so that $K = (K_y^2 + K_z^2)^{1/2} = \pi(1 + \alpha^2)^{1/2}$. Note that for a classical laminar convection [where there are no terms $\propto \epsilon$ in Eq. (6), and $\alpha = 1/\sqrt{2}$] with the vertical boundary conditions given by Eqs. (11)–(13), the maximum growth rate of the convective instability is attained at the nondimensional wavenumber $K_y = \pi/\sqrt{2}$.

Let us consider convective turbulence, and the large-scale properties of the system are described by the mean-field equations (5) and (6), where $\epsilon \neq 0$. Substituting solution (14)–(16) into linearized

Eqs. (5) and (6), we obtain the nondimensional growth rate γ_{inst} of the large-scale convective-wind instability (see Appendix B),

$$\gamma_{inst} = \frac{\alpha}{(1 + \alpha^2)^{1/2}} \left[Ra_T + \frac{\sigma \pi^2}{2\epsilon} (1 - \alpha^2) \right]^{1/2} - \pi^2 (1 + \alpha^2). \tag{17}$$

Here, we consider the case when the turbulent Prandtl number $Pr_T = 1$. The condition $\gamma_{inst} = 0$ yields the critical effective Rayleigh number Ra_T^{cr} required for the excitation of the large-scale convective-wind instability,

$$Ra_T^{cr} = \frac{\pi^4 (1 + \alpha^2)^3}{\alpha^2} \left[1 - \frac{\sigma (1 - \alpha^2)}{2\pi^2 \epsilon (1 + \alpha^2)^3} \right]. \tag{18}$$

Note that Eq. (18) is valid for arbitrary turbulent Prandtl number Pr_T .

Equations (17) and (18) at $\epsilon = 0$ (i.e., $\sigma = 0$) describe the classical laminar convection, where the effective Rayleigh number Ra_T based on the turbulent transport coefficients should be replaced by the Rayleigh number Ra based on the molecular transport coefficients. It follows from Eq. (18) that the critical effective Rayleigh number required for the large-scale convective-wind instability is strongly reduced in turbulence (for perturbations with $\alpha < 1$). This is due to the modification of the turbulent heat flux by the nonuniform motions. This effect will be discussed in Sec. IV, where the results of mean-field simulations are described. Note that Eq. (17) agrees with Eq. (4) for $Ra_T \rightarrow 0$.

In Fig. 2, we show the critical effective Rayleigh number Ra_T^{cr} vs the parameter α for different values of the parameter $\sigma = 3(u_c/u_0)^3$, while in Fig. 3 we plot the critical effective Rayleigh number Ra_T^{cr} as the function of the parameter ϵ/σ for different values of the parameter α . The classical convection corresponds to $\sigma = 0$ when the turbulent integral scale ℓ_0 vanishes. The increase in the parameter σ decreases the critical effective Rayleigh number required for the large-scale convective-wind instability. This tendency is also seen in Fig. 4, where we plot the non-dimensional growth rate γ_{inst} of the large-scale convective-wind instability vs the effective Rayleigh numbers Ra_T for different values of the parameter σ . In Fig. 5, we show the non-dimensional growth rate γ_{inst} of the large-scale convective-wind instability vs α for different effective Rayleigh numbers Ra_T . The thick lines in Fig. 5 correspond to turbulent convection, while the thin lines correspond to the classical laminar convection. In the classical laminar

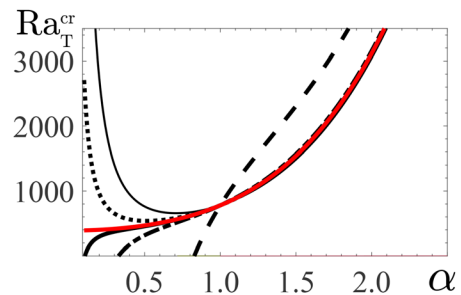


FIG. 2. The critical effective Rayleigh number Ra_T^{cr} vs the parameter α for $\epsilon = 10^{-2}$ and different values of the parameter $\sigma = 3$ (dashed); 0.3 (dashed-dotted); 0.206 (solid thick); 0.197 (red); 0.15 (dotted); and for the classical laminar convection with $\sigma = 0$ (solid thin).

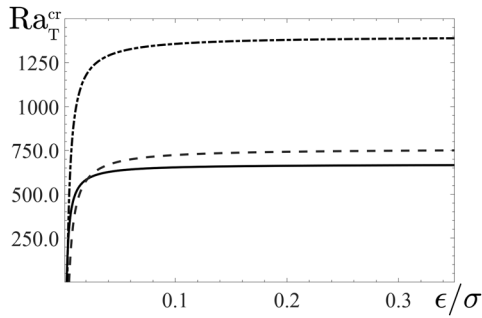


FIG. 3. The critical effective Rayleigh number Ra_T^{cr} vs the parameter ϵ/σ and different values of the parameter $\alpha = 0.3$ (dashed-dotted), 0.5 (dashed), and 0.8 (solid).

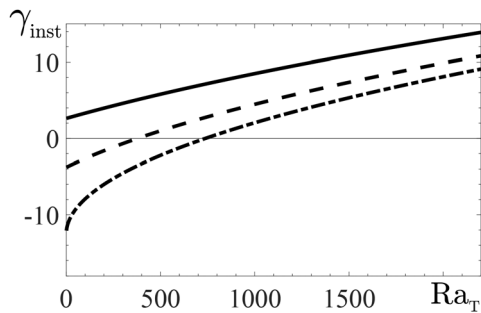


FIG. 4. The non-dimensional growth rate γ_{inst} of the large-scale convective-wind instability vs the effective Rayleigh numbers Ra_T for $\alpha = 0.5$, $\epsilon = 10^{-2}$ and different values of the parameter $\sigma = 3$ (solid); 1 (dashed); and for the classical convection with $\sigma = 0$ (dashed-dotted).

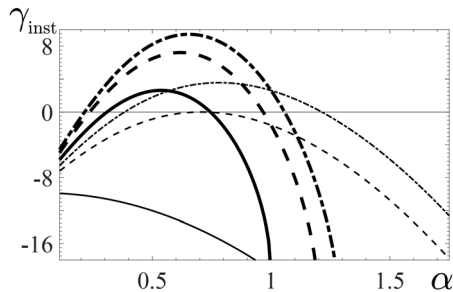


FIG. 5. The non-dimensional growth rate γ_{inst} of the large-scale convective-wind instability vs α for $\sigma = 3$, $\epsilon = 10^{-2}$ and different effective Rayleigh numbers $Ra_T = 1000$ (dashed-dotted thick); 657.5 (dashed thick); 0.5 (solid-thick); and for the classical convection with $\sigma = 0$ and different Rayleigh number $Ra_T = 1000$ (dashed-dotted thin); 657.5 (dashed thin); and 0.5 (solid-thin).

convection the maximum growth rate of the convective instability is attained when α tends to 1, while in the turbulent convection the convective-wind instability is more effective when α tends to $1/2$.

In Fig. 6, we plot the nondimensional growth rate $\gamma_{inst}^* = 10 \gamma_{inst} \epsilon^{1/2}$ of the large-scale convective-wind instability vs L_z/ℓ_0 for different values of the effective Rayleigh number. We show the growth rate γ_{inst}^* instead of γ_{inst} by the following reasons. Since the

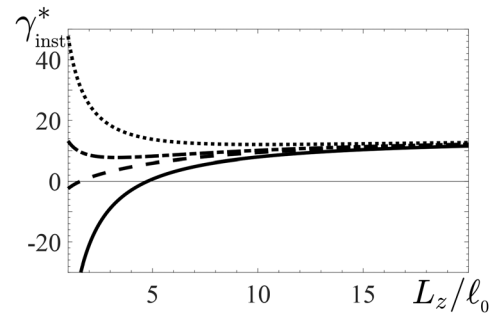


FIG. 6. The non-dimensional growth rate $\gamma_{inst}^* = 10 \gamma_{inst} \epsilon^{1/2}$ of the large-scale convective-wind instability vs L_z/ℓ_0 for $\alpha = 0.5$ and different effective Rayleigh number $Ra_T = 2000$ (dotted); 1000 (dashed-dotted); 657.5 (dashed); and 0.5 (solid).

growth rate of the large-scale convective-wind instability is measured in the units of ν_T/L_z^2 and the turbulent viscosity $\nu_T = u_0 \ell_0/3$ is proportional to the integral turbulence scale ℓ_0 , we show the nondimensional growth rate γ_{inst}^* which is measured in the units which are independent of ℓ_0 . Figure 6 demonstrates that when the effective Rayleigh number is not large, the separation of scales L_z/ℓ_0 between the size of the convective layer and the integral scale of turbulence should be large (more than 5–10) to observe the large-scale convective-wind instability and formation of large-scale coherent structures.

IV. RESULTS OF THE MEAN-FIELD NUMERICAL SIMULATIONS

In this section, we study nonlinear evolution of the convective-wind instability by means of the mean-field numerical simulations, where we solve numerically Eqs. (5) and (6) for the periodic boundary conditions in the horizontal directions (along the x and y axes). We use two kinds of the vertical boundary conditions for the velocity field: (i) stress-free boundary conditions corresponding to the free vertical boundaries and (ii) no-slip boundary conditions corresponding to the rigid vertical boundaries. The boundary conditions for the potential temperature in the vertical direction are $\tilde{\Theta}(t, z = 0) = \tilde{\Theta}(t, z = 1) = 0$.

Simulations are performed using the ANSYS FLUENT code (version 19.2) (<https://lawn-mower-manual.com/html/ansys-fluent-theory-guide-2020>) which applies the Final Volume method in the 3D box $L_x = L_z = 1$ and $L_y = 2$. The additional terms $\propto \epsilon$ in the divergence of the turbulent heat flux are implemented into the code as the source terms in the potential temperature equation (6).

The simulations are performed with the spatial resolution $100 \times 200 \times 100$ in x , y , and z directions, respectively. A sensitivity check has been also made for the spatial resolution $150 \times 300 \times 150$. For both cases, similar results for velocity and potential temperature have been obtained. In all simulations, we use a time step of 10^{-3} . A sensitivity check has been made for time steps as well. Time steps of 10^{-3} and 2×10^{-3} have been tested, and a maximum error of 0.05% at velocity and potential temperature using these time steps has been obtained. In addition, a convergence error was set to be less than 10^{-6} .

The parameters for the simulations are the following: the turbulent Prandtl number $Pr_T = 1$, the ratio $u_c/u_0 = 1$, the effective Rayleigh number varies from $Ra_T = 0.5$ to $Ra_T = 2700$, and the scale separation parameter ϵ varies in the range $(0.5-2) \times 10^{-3}$. Different theoretical and numerical studies show that the turbulent Prandtl

number Pr_T for large Reynolds numbers in isothermal and convective turbulence is of the order of 1 (see Refs. 50–54) while in stably stratified turbulence the turbulent Prandtl number can be much larger than 1 only for large Richardson numbers (see Refs. 55–61). The variations of the parameter $\epsilon = (0.5\text{--}2.5) \times 10^{-3}$ (characterizing the separation of scales between the height L_z of the convective layer and the integral turbulence scale ℓ_0) corresponds to variations of the ratio $L_z/\ell_0 = 12\text{--}26$. The choice of the other parameters is discussed below and in Sec. V.

A. Numerical simulations with the stress-free vertical boundary conditions

Let us discuss the results of the mean-field numerical simulations which take into account the modification of the turbulent heat flux by the non-uniform motions [described by the terms $\propto \epsilon$ in Eq. (6)]. Here we discuss the numerical results for the stress-free boundary conditions in the vertical direction and for the following initial conditions:

$$\tilde{U}_z(t = 0, z) = U_0 \sin(\pi z) \cos(\alpha\pi y), \tag{19}$$

$$\tilde{U}_y(t = 0, z) = -\alpha^{-1} U_0 \cos(\pi z) \sin(\alpha\pi y), \tag{20}$$

$$\tilde{U}_x(t = 0, z) = 0, \tag{21}$$

$$\tilde{\Theta}(t = 0, z) = \Theta_0 \sin(\pi z) \cos(\alpha\pi y), \tag{22}$$

[see analytical solution (14)–(16)], where U_0 is initial amplitude of the nondimensional mean vertical velocity. In the mean-field numerical simulations, we use the parameters $U_0 = 10^{-4}$ and $\alpha = 0.35$. In some simulations we also use $U_0 = 0.23$ to avoid a long transition range. The obtained results are nearly independent of parameter U_0 .

In Figs. 7 and 8, we show the time evolution of the maximum velocity $\tilde{U}_{max}(t)$ for different effective Rayleigh numbers varying from $Ra_T = 0.5$ to 1800 and different values of the parameter ϵ (which

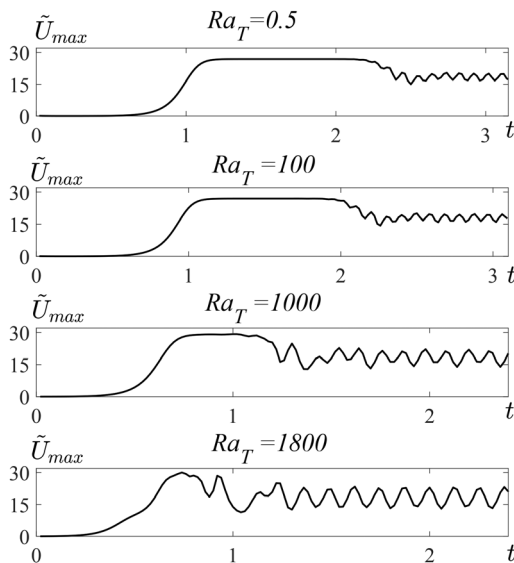


FIG. 7. Time evolution of the maximum velocity $\tilde{U}_{max}(t)$ at $\epsilon = 2.5 \times 10^{-3}$ and different values of the effective Rayleigh number Ra_T for the stress-free boundary conditions.

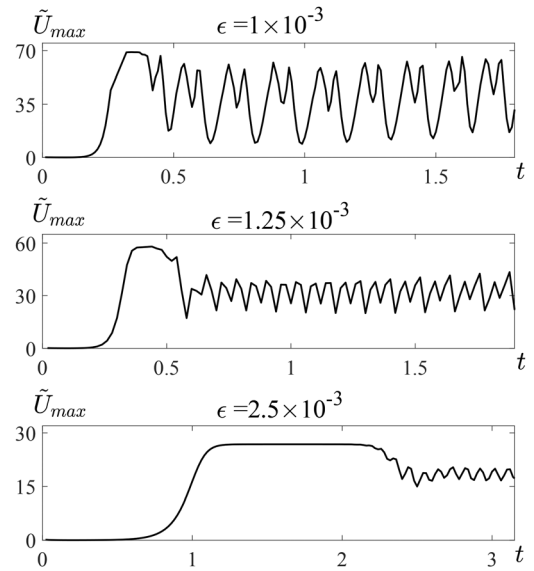


FIG. 8. Time evolution of the maximum velocity $\tilde{U}_{max}(t)$ at $Ra_T = 0.5$ and different values of ϵ for the stress-free boundary conditions.

characterizes scale separation between the vertical size L_z of the computational domain and the integral turbulence scale ℓ_0). During the linear stage of the large-scale convective-wind instability, the maximum velocity $\tilde{U}_{max}(t)$ grows in time exponentially. The instability is saturated by the nonlinear effects. For smaller values of the parameter ϵ (i.e., for larger values of the parameter L_z/ℓ_0), after the stationary stage when the maximum velocity $\tilde{U}_{max}(t)$ reaches the constant, nonlinear oscillations of the maximum velocity $\tilde{U}_{max}(t)$ are observed. With the increase in the effective Rayleigh number Ra_T , the duration of the stationary stage decreases (see Fig. 7). The values of the maximum velocity \tilde{U}_{max} at the stationary stage are nearly independent of the effective Rayleigh number Ra_T (see Fig. 7), but \tilde{U}_{max} at the stationary stage strongly depends on the scale separation parameter ϵ (see Fig. 8).

We show also the velocity patterns in the yz plane at the stationary stage [Fig. 9(a)]. Since the potential temperature is measured in the units of $L_z N^2 Pr_T / \beta = Ra_T \nu_T^2 / (\beta L_z^2)$, we show in Fig. 9(b) the pattern of the normalized deviations of the potential temperature $\tilde{\Theta} Ra_T$ from the equilibrium potential temperature in the basic reference state. Figure 9 is for the stress-free vertical boundary conditions, $\epsilon = 2.5 \times 10^{-3}$ and the effective Rayleigh number, $Ra_T = 0.5$. All fields in Fig. 9 are normalized by their maximum values.

Figures 9(a) and 9(b) demonstrate the four-cell patterns of the velocity and potential temperature, where the two-cell patterns are located in both, the upper and bottom parts of Fig. 9. Remarkably, the large-scale circulations exist even below the threshold of the laminar convection. The main reason is that turbulence with nonuniform large-scale flows contributes to the turbulent heat flux. In particular, nonuniform large-scale flows produce anisotropic velocity fluctuations modifying the turbulent heat flux. As the result, the evolutionary equation (6) for the potential temperature $\tilde{\Theta}$ contains the new terms proportional to the spatial derivatives of the mean velocity field \tilde{U} (see the terms $\propto \epsilon$). For the stress-free boundary conditions and different

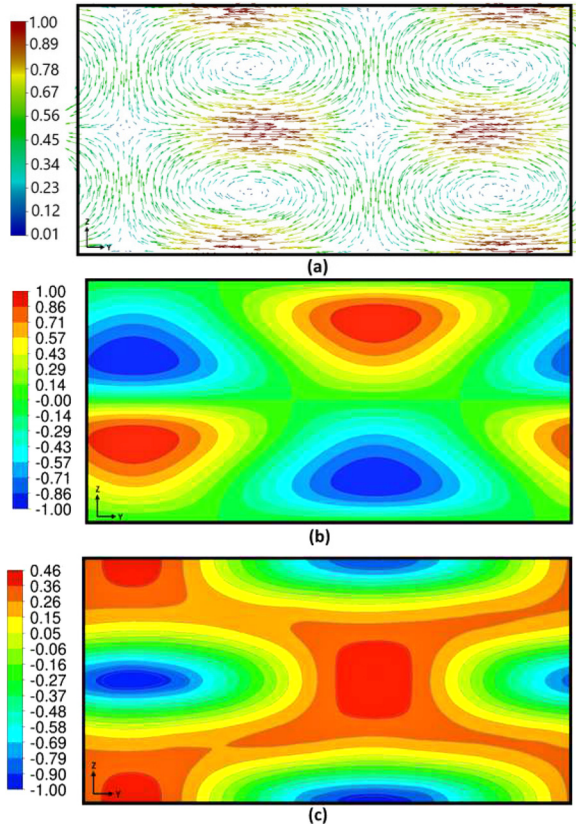


FIG. 9. The velocity patterns at the stationary stage (a), the potential temperature deviations $\bar{\Theta}$ from the equilibrium potential temperature in the basic reference state (b) and the total vertical gradient of the mean potential temperature $(\nabla_z \bar{\Theta} - 1) Ra_T$ (c) in yz plane for the stress-free vertical boundary conditions for $\epsilon = 2.5 \times 10^{-3}$ and the effective Rayleigh number $Ra_T = 0.5$. All fields are normalized by their maximum values.

effective Rayleigh numbers varying from $Ra_T = 0.5$ to $Ra_T = 1800$, we observe the same four-cell flow patterns which is seen in Fig. 9.

Since the total gradient of the potential temperature is the sum of the equilibrium constant gradient of the potential temperature $\nabla_z \bar{T}_{eq}$ (which is negative as usual for a convection) and the gradient of the potential temperature $\nabla_z \bar{\Theta}$, we show in Fig. 9(c) the pattern of the normalized total vertical gradient of the mean potential temperature, $(\nabla_z \bar{\Theta} - 1) Ra_T$ that includes the equilibrium constant gradient of the potential temperature $\nabla_z \bar{T}_{eq}$. The normalized vertical gradient of the mean potential temperature, $(\nabla_z \bar{\Theta} - 1) Ra_T$ describes convection. Figure 9(c) demonstrates existence of the regions with the positive gradient of the potential temperature $(\nabla_z \bar{\Theta} - 1) Ra_T$. This implies that these regions are stably stratified. Such effects have been previously observed in experiments^{14,48} and direct numerical simulations (DNS)^{32–34,49} of turbulent convection.

The existence of the regions with the positive gradient of the potential temperature inside the large-scale circulation can be explained as follows. The total vertical heat flux F_z^{tot} is the sum of the mean vertical heat flux $\bar{U}_z \bar{\Theta}$ of the large-scale circulation, the vertical turbulent heat flux $F_z^* = -\kappa_T \nabla_z \bar{\Theta}$ and the new turbulent heat flux

$F_z^{new} = -\tau_0 F_z^* \text{div } \bar{U}_\perp$ (these fluxes are written here in the dimensional form), i.e.,

$$F_z^{tot} = \bar{U}_z \bar{\Theta} - \kappa_T \nabla_z \bar{\Theta} - \tau_0 F_z^* \text{div } \bar{U}_\perp. \quad (23)$$

Note that the last term in Eq. (3) does not have the vertical component. Equation (23) yields the vertical gradient of the mean potential temperature $\nabla_z \bar{\Theta}$,

$$\nabla_z \bar{\Theta} = \frac{\bar{U}_z \bar{\Theta} - F_z^{tot}}{\kappa_T (1 - \tau_0 \text{div } \bar{U}_\perp)}. \quad (24)$$

In the regions inside the large-scale circulation where $\bar{U}_z \bar{\Theta} > F_z^{tot}$, the vertical gradient $\nabla_z \bar{\Theta}$ is positive, while when $\bar{U}_z \bar{\Theta} < F_z^{tot}$, the vertical gradient $\nabla_z \bar{\Theta}$ is negative. Note that usually $\tau_0 |\text{div } \bar{U}_\perp| < 1$. This explains the existence of the regions with the positive gradient of the potential temperature inside the large-scale circulation in a turbulent convection.

B. Numerical simulations with the no-slip vertical boundary conditions

In this section, we use the no-slip boundary conditions for the velocity field in the vertical direction,

$$\tilde{U}(t, z=0) = \tilde{U}(t, z=1) = 0. \quad (25)$$

For the classical laminar convection with the no-slip boundary conditions [where there are no terms $\propto \epsilon$ in Eq. (6)], the critical Rayleigh number required for the excitation of convection is $Ra_{cr} \approx 1708$.^{44–47}

Let us discuss the results of the mean-field numerical simulations for the case which takes into account the modification of the turbulent heat flux by the nonuniform motions [described by the terms $\propto \epsilon$ in Eq. (6)]. In Figs. 10–12, we plot time evolution of the maximum velocity $\tilde{U}_{max}(t)$ for different effective Rayleigh numbers varying from

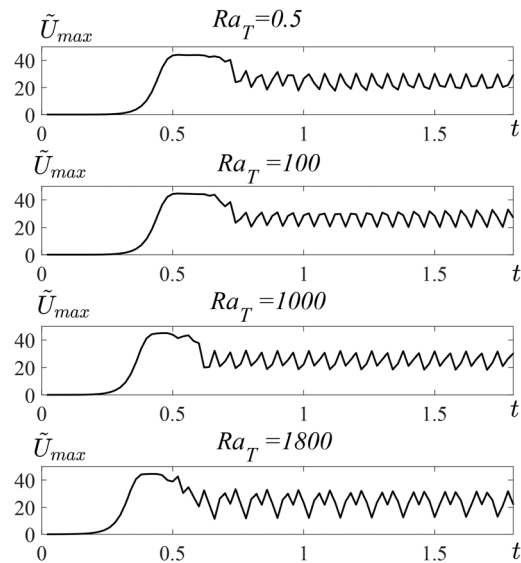


FIG. 10. Time evolution of the maximum velocity $\tilde{U}_{max}(t)$ at $\epsilon = 10^{-3}$ and different values of the effective Rayleigh number Ra_T for the no-slip boundary conditions.

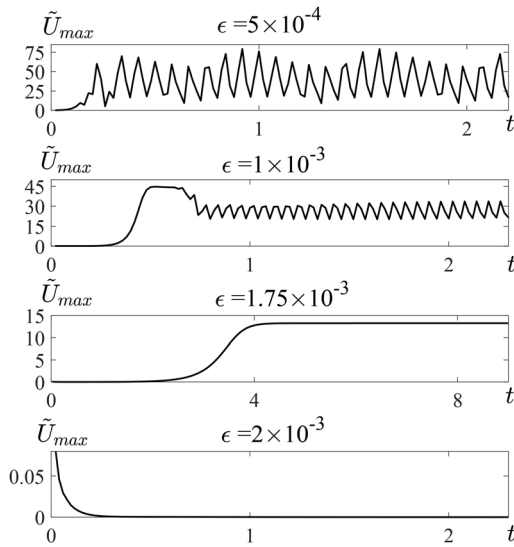


FIG. 11. Time evolution of the maximum velocity $\tilde{U}_{max}(t)$ at $Ra_T = 100$ and different values of ϵ for the no-slip boundary conditions.

$Ra_T = 0.5$ to 1800 and different values of the parameter ϵ . The large-scale convective-wind instability is excited when the parameter $\epsilon \leq 1.75 \times 10^{-3}$. After the exponential growth of the maximum velocity $\tilde{U}_{max}(t)$, there is a saturation stage of the convective-wind instability. We also observe the nonlinear oscillations of the maximum velocity $\tilde{U}_{max}(t)$ which follow after the stationary stage when the maximum velocity $\tilde{U}_{max}(t)$ reaches the constant. The characteristic duration of the stationary stage decreases with increase in the effective Rayleigh number Ra_T (see Fig. 10). As well as for the stress-free vertical boundary conditions, the maximum velocity $\tilde{U}_{max}(t)$ in saturation

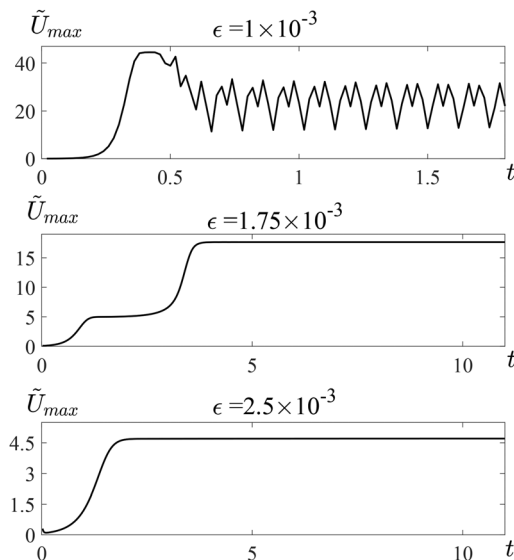


FIG. 12. Time evolution of the maximum velocity $\tilde{U}_{max}(t)$ at $Ra_T = 1800$ and different values of ϵ for the no-slip boundary conditions.

depends strongly on the scale separation parameter ϵ (see Figs. 11 and 12), and it is nearly independent of the effective Rayleigh number (see Fig. 10).

We also show the velocity patterns [Figs. 13(a) and 14(a)] in yz plane at the stationary stage, the potential temperature deviations $\Theta - Ra_T$ from the equilibrium potential temperature in the basic reference state [Figs. 13(b) and 14(b)] and the total vertical gradient of the mean potential temperature $(\nabla_z \bar{\Theta} - 1) Ra_T$ [Figs. 13(c) and 14(b)]. These figures are for the no-slip vertical boundary conditions at the effective Rayleigh number $Ra_T = 1800$, and for two values of the parameter $\epsilon = 1.75 \times 10^{-3}$ (Fig. 13) and $\epsilon = 2.5 \times 10^{-3}$ (Fig. 14).

As well as for the stress-free vertical boundary conditions, the large-scale circulations form even below the threshold of the laminar convection for the case of the no-slip boundary conditions. However, for the no-slip vertical boundary conditions we see some differences. In particular, increasing the parameter ϵ from $\epsilon = 1.75 \times 10^{-3}$ to $\epsilon = 2.5 \times 10^{-3}$, we observe a transition from the four-cell flow patterns [see Figs. 13(a) and 13(b)] to the two-cell patterns [see Figs. 14(a) and 14(b)]. As well as for the stress-free vertical boundary conditions, Figs. 13(c) and 14(c) also show the regions with the positive total

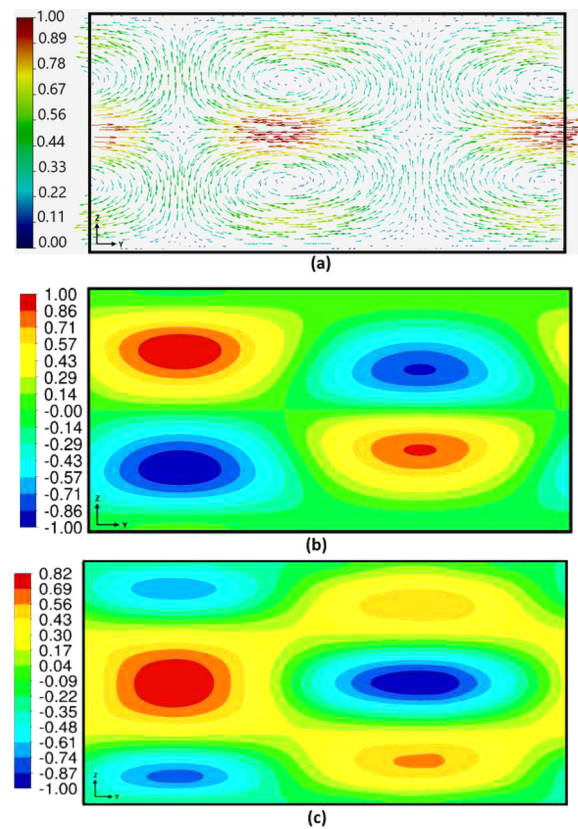


FIG. 13. The velocity patterns at the stationary stage (a), the potential temperature deviations $\Theta - Ra_T$ from the equilibrium potential temperature in the basic reference state (b) and the total vertical gradient of the mean potential temperature $(\nabla_z \bar{\Theta} - 1) Ra_T$ (c) in yz plane for the no-slip vertical boundary conditions for $\epsilon = 1.75 \times 10^{-3}$ and the effective Rayleigh number $Ra_T = 1800$. All fields are normalized by their maximum values.

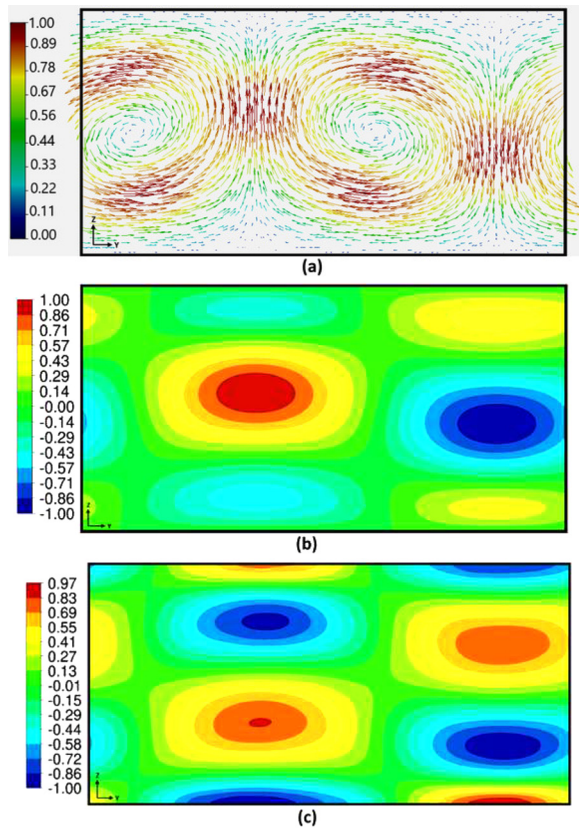


FIG. 14. The velocity patterns at the stationary stage (a), the potential temperature deviations $\tilde{\Theta} \text{Ra}_T$ from the equilibrium potential temperature in the basic reference state (b) and the total vertical gradient of the mean potential temperature $(\nabla_z \tilde{\Theta} - 1) \text{Ra}_T$ (c) in yz plane for the no-slip vertical boundary conditions for $\epsilon = 2.5 \times 10^{-3}$ and the effective Rayleigh number $\text{Ra}_T = 1800$. All fields are normalized by their maximum values.

gradient of the potential temperature $(\nabla_z \tilde{\Theta} - 1) \text{Ra}_T$, which correspond to the stably stratified flows. This study demonstrates that dependence on the vertical boundary conditions (the stress-free or no-slip boundary conditions) is not essential.

V. DISCUSSION

Let us discuss the novelty aspects and significance of the obtained results. The effect of modification of the turbulent heat flux by nonuniform large-scale motions in turbulent convection was investigated analytically in Ref. 42, where the turbulent heat flux F given by Eq. (3) was derived. This new effect causes an excitation of the convective-wind instability. The estimate for the growth rate of the convective-wind instability [see Eq. (4)] was obtained for the case when the effective Rayleigh number vanishes, $\text{Ra}_T \rightarrow 0$.⁴² The linear stage of the convective-wind instability was numerically studied in Ref. 44 for different conditions. Applications of these results to atmospheric turbulence were discussed in Ref. 43, where the theoretical predictions⁴² were compared with observational characteristics of the cloud convective cells.

In the present paper, we have generalized Eq. (4) for the growth rate of the convective-wind instability for arbitrary effective Rayleigh

numbers [see Eq. (17)]. This allows us to obtain equation for the critical effective Rayleigh number required for the excitation of the large-scale convective-wind instability [see Eq. (18)]. This equation explains why the large-scale circulation can be formed in turbulent convection even for very low effective Rayleigh numbers. This result has been confirmed by the mean-field simulations performed in the present study.

We have shown that the convective-wind instability strongly depends on the scale separation parameter ϵ characterizing the separation of scales between the height of the convective layer L_z and the integral turbulence scale ℓ_0 . In the mean-field numerical simulations, the parameter ϵ varies in the range $(0.5-2.5) \times 10^{-3}$, which corresponds to variations of the separation of scales L_z/ℓ_0 in the range 12–26. Any mean-field theory is usually valid when the integral turbulence scale is much less than the characteristic scale of the mean-field variations, that is consistent with these values L_z/ℓ_0 . Also direct measurements in laboratory experiments in turbulent convection by measuring of the two-point correlation function of velocity fluctuations (which allow us to determine the integral scale of turbulence) are consistent with these values of L_z/ℓ_0 (see Refs. 25 and 26).

Direct numerical simulations (DNS) cannot be performed for very large Reynolds numbers (i.e., for Reynolds numbers based on integral scale and maximum turbulent velocity which are larger than 10^4), while in many applications, e.g., in atmospheric and astrophysical turbulent flows, characteristic Reynolds numbers are much larger than 10^4 . In this case, mean-field simulations based on nonlinear mean-field equations [where turbulent effects are described by means of effective (turbulent) transport coefficients and modified turbulent heat flux] can be very useful. The mean-field numerical simulations demonstrate existence of the local regions with the positive vertical gradient of the potential temperature inside the large-scale circulations. In the present study we explain this effect [see Eqs. (23) and (24) and corresponding discussion after these equations]. This effect was previously observed in laboratory experiments (see, e.g., Refs. 14 and 48) as well as in DNS of turbulent convection (see, e.g., Refs. 32–34).

In view of applications, the obtained results are relevant to large-scale convective cells (the cloud cells) observed in the atmospheric turbulent convection without strong mean wind. They are formed in a convective boundary layer with a depth of about 1 to 3 km and have aspect ratios $L_z/L_{\text{hor}} \approx 0.05-1$ (see, e.g., Ref. 39), where L_{hor} and L_z are the horizontal and vertical sizes of convective cells. The ratio of the minimum size of the convective cells to the maximum scale of turbulent motions is $L_{\text{min}}/\ell_0 = 5-20$. This implies that the parameter ϵ for the observed convective cells ranges from 10^{-3} to 10^{-2} . The characteristic time of formation of the convective cells ($\tau_{\text{form}} \sim \tau_0/\gamma_{\text{inst}}$) in the atmospheric turbulent convection varies from 1 to 3 h. Here γ_{inst} is the nondimensional growth rate of the instability [see Eq. (17)].

Turbulent velocity u_0 at the lower part of the surface convective layer, where the turbulence production is mainly due to the large-scale shear motions, is of the order of $u_0 \sim (2-4) u_*$, where u_* is the friction velocity. At the upper part of the surface convective layer, where production of the turbulence is mainly due to the buoyancy, is of the order of the turbulent convective velocity $u_c = (\beta F_z^* \ell_0)^{1/3}$ (see, e.g., Ref. 7), which implies that $u_0/u_c \sim 1$.

VI. CONCLUSIONS

In the present paper, we study formation and nonlinear evolution of large-scale circulations in turbulent convection by means of the

mean-field numerical simulations. We use periodic horizontal boundary conditions, and stress-free or no-slip vertical boundary conditions. We have taken into account the effect of strong modification of the turbulent heat flux by nonuniform large-scale motions which generate anisotropic velocity fluctuations. The performed mean-field numerical simulations have shown that this effect strongly reduces the critical Rayleigh number (based on the eddy viscosity and turbulent temperature diffusivity) required for onset of the large-scale convective instability and formation of large-scale semi-organized coherent structures (large-scale circulations). The onset of this instability and the level of the mean velocity at saturation strongly depend on the scale separation ratio between the height of the convective layer and the integral scale of turbulence. The simulations demonstrate the existence of the local regions with the positive vertical gradient of the potential temperature inside the large-scale circulations. The latter implies that these regions are stably stratified.

ACKNOWLEDGMENTS

The authors benefited from stimulating discussions of various aspects of turbulent convection with A. Brandenburg, F. H. Busse, P. J. Käpylä, and S. Zilitinkevich. This research was supported in part by the Israel Ministry of Science and Technology (Grant No. 3-16516) and the PAZY Foundation of the Israel Atomic Energy Commission (Grant No. 122-2020).

AUTHOR DECLARATIONS

Conflict of Interest

The authors have no conflicts to disclose.

Author Contributions

Gali Orian: Investigation (equal). **Arieh Asulin:** Investigation (equal). **Evgeny Tkachenko:** Investigation (equal). **Nathan Kleeorin:** Conceptualization (equal); Investigation (equal); Writing – original draft (equal). **Avi Levy:** Conceptualization (equal); Investigation (equal); Writing – original draft (equal). **Igor Rogachevskii:** Conceptualization (equal); Investigation (equal); Writing – original draft (equal).

DATA AVAILABILITY

The data that support the findings of this study are available from the corresponding author upon reasonable request.

APPENDIX A: DERIVATION OF EQ. (6)

In this appendix, we derive Eq. (6) for the mean potential temperature. To this end, we use Eq. (3) for the turbulent heat flux F with the additional terms caused by the non-uniform mean flows. We determine $\text{div } F$ by assuming that the non-dimensional total vertical heat flux $F_z^{\text{tot}} = F_z^* + \bar{U}_z \bar{\Theta}$ is constant. This yields

$$\begin{aligned} \nabla \cdot F = & -\kappa_T \Delta \bar{\Theta} - \tau_0 \left[(F_z^{\text{tot}} - \bar{U}_z \bar{\Theta}) \left(\frac{\Delta}{2} - \nabla_z^2 \right) \bar{U}_z \right. \\ & + \frac{1}{2} (\nabla_z \bar{U}_x - \nabla_x \bar{U}_z) \nabla_x (\bar{U}_z \bar{\Theta}) + \frac{1}{2} (\nabla_z \bar{U}_y - \nabla_y \bar{U}_z) \\ & \left. \times \nabla_y (\bar{U}_z \bar{\Theta}) + (\nabla_z \bar{U}_z) \nabla_z (\bar{U}_z \bar{\Theta}) \right]. \end{aligned} \quad (\text{A1})$$

Using Eqs. (2) and (A1), written in non-dimensional form (see definitions of the non-dimensional variables and the key parameters in Sec. III), we obtain Eq. (6).

APPENDIX B: DERIVATION OF EQ. (17)

In this appendix, we derive Eq. (17) for growth rate of the large-scale convective-wind instability. To this end, we use linearized non-dimensional equations (5) and (6), calculate $[\mathbf{V} \times (\mathbf{V} \times \tilde{\mathbf{U}})]_z$ using the linearized Eq. (5) to exclude the pressure term, and seek for solution of the obtained equations in the following form: $\tilde{\mathbf{U}}(t, \mathbf{x}) = \tilde{\mathbf{U}}_0 \exp[i(\gamma_{\text{inst}} t + \mathbf{K} \cdot \mathbf{x})]$ and $\tilde{\Theta}(t, \mathbf{x}) = \tilde{\Theta}_0 \exp[i(\gamma_{\text{inst}} t + \mathbf{K} \cdot \mathbf{x})]$. This yields the following system of equations:

$$(\gamma_{\text{inst}} + K^2) \tilde{U}_z + \text{Ra}_T \left(\frac{K_z^2}{K^2} - 1 \right) \tilde{\Theta} = 0, \quad (\text{B1})$$

$$\left[1 + \frac{\sigma}{\epsilon \text{Ra}_T} \left(K_z^2 - \frac{K^2}{2} \right) \right] \tilde{U}_z - (\gamma_{\text{inst}} + K^2) \tilde{\Theta} = 0, \quad (\text{B2})$$

where $\sigma = 3(u_c/u_0)^3$, and we consider, for simplicity, the case when the turbulent Prandtl number $\text{Pr}_T = 1$. Equations (B1) and (B2) yield the non-dimensional growth rate (17) of the large-scale convective-wind instability, where $K_z = \pi$ and $K \equiv |\mathbf{K}| = \pi(1 + \alpha^2)^{1/2}$.

REFERENCES

- ¹S. S. Zilitinkevich, *Turbulent Penetrative Convection* (Avebury Technical, Aldershot, 1991).
- ²E. S. C. Ching, *Statistics and Scaling in Turbulent Rayleigh-Bénard Convection* (Springer, Singapore, 2014).
- ³E. D. Siggia, “High Rayleigh number convection,” *Annu. Rev. Fluid Mech.* **26**, 137 (1994).
- ⁴G. Ahlers, S. Grossmann, and D. Lohse, “Heat transfer and large scale dynamics in turbulent Rayleigh-Bénard convection,” *Rev. Mod. Phys.* **81**, 503 (2009).
- ⁵D. Lohse and K.-Q. Xia, “Small-scale properties of turbulent Rayleigh-Bénard convection,” *Annu. Rev. Fluid Mech.* **42**, 335 (2010).
- ⁶J. S. Turner, *Buoyancy Effects in Fluids* (Cambridge University Press, Cambridge, 1973).
- ⁷A. S. Monin and A. M. Yaglom, *Statistical Fluid Mechanics* (MIT Press, Cambridge, MA, 1975), Vol. 2.
- ⁸I. Rogachevskii, *Introduction to Turbulent Transport of Particles, Temperature and Magnetic Fields* (Cambridge University Press, Cambridge, 2021).
- ⁹E. Bodenschatz, W. Pesch, and G. Ahlers, “Recent developments in Rayleigh-Bénard convection,” *Annu. Rev. Fluid Mech.* **32**, 709 (2000).
- ¹⁰Q. Zhou and K.-Q. Xia, “The mixing evolution and geometric properties of a passive scalar field in turbulent Rayleigh-Bénard convection,” *New J. Phys.* **12**, 083029 (2010).
- ¹¹R. Krishnamurti and L. N. Howard, “Large-scale flow generation in turbulent convection,” *Proc. Natl. Acad. Sci. U. S. A.* **78**, 1981 (1981).
- ¹²M. Sano, X. Z. Wu, and A. Libchaber, “Turbulence in helium-gas free convection,” *Phys. Rev. A* **40**, 6421 (1989).
- ¹³S. Ciliberto, S. Cioni, and C. Laroche, “Large-scale flow properties of turbulent thermal convection,” *Phys. Rev. E* **54**, R5901 (1996).
- ¹⁴J. J. Niemela, L. Skrbek, K. R. Sreenivasan, and R. J. Donnelly, “The wind in confined thermal convection,” *J. Fluid Mech.* **449**, 169 (2001).
- ¹⁵J. J. Niemela and K. R. Sreenivasan, “Rayleigh-number evolution of large-scale coherent motion in turbulent convection,” *Europhys. Lett.* **62**, 829 (2003).
- ¹⁶U. Burr, W. Kinzelbach, and A. Tsinober, “Is the turbulent wind in convective flows driven by fluctuations?,” *Phys. Fluids* **15**, 2313 (2003).

- ¹⁷K.-Q. Xia, C. Sun, and S.-Q. Zhou, "Particle image velocimetry measurement of the velocity field in turbulent thermal convection," *Phys. Rev. E* **68**, 066303 (2003).
- ¹⁸H. D. Xi, S. Lam, and X. Q. Xia, "From laminar plumes to organized flows: The onset of large-scale circulation in turbulent thermal convection," *J. Fluid Mech.* **503**, 47 (2004).
- ¹⁹X. D. Shang, X. L. Qiu, P. Tong, and X. Q. Xia, "Measurements of the local convective heat flux in turbulent Rayleigh-Bénard convection," *Phys. Rev. E* **70**, 026308 (2004).
- ²⁰D. Funfschilling and G. Ahlers, "Plume motion and large-scale circulation in a cylindrical Rayleigh-Bénard cell," *Phys. Rev. Lett.* **92**, 194502 (2004).
- ²¹E. Brown, A. Nikolaenko, and G. Ahlers, "Orientation changes of the large-scale circulation in turbulent Rayleigh-Bénard convection," *Phys. Rev. Lett.* **95**, 084503 (2005).
- ²²A. Liberzon, B. Lüthi, M. Guala, W. Kinzelbach, and A. Tsinober, "Experimental study of the structure of flow regions with negative turbulent kinetic energy production in confined three-dimensional shear flows with and without buoyancy," *Phys. Fluids* **17**, 095110 (2005).
- ²³D. Funfschilling, E. Brown, and G. Ahlers, "Torsional oscillations of the large-scale circulation in turbulent Rayleigh-Bénard convection," *J. Fluid Mech.* **607**, 119 (2008).
- ²⁴A. Eidelman, T. Elperin, N. Kleeorin, A. Markovich, and I. Rogachevskii, "Hysteresis phenomenon in turbulent convection," *Exp. Fluids* **40**, 723 (2006).
- ²⁵M. Bukai, A. Eidelman, T. Elperin, N. Kleeorin, I. Rogachevskii, and I. Sapir-Katiraie, "Effect of large-scale coherent structures on turbulent convection," *Phys. Rev. E* **79**, 066302 (2009).
- ²⁶M. Bukai, A. Eidelman, T. Elperin, N. Kleeorin, I. Rogachevskii, and I. Sapir-Katiraie, "Transition phenomena in unstably stratified turbulent flows," *Phys. Rev. E* **83**, 036302 (2011).
- ²⁷T. Hartlep, A. Tilgner, and F. H. Busse, "Large-scale structures in Rayleigh-Bénard convection at high Rayleigh numbers," *Phys. Rev. Lett.* **91**, 064501 (2003).
- ²⁸A. Parodi, J. von Hardenberg, G. Passoni, A. Provenzale, and E. A. Spiegel, "Clustering of plumes in turbulent convection," *Phys. Rev. Lett.* **92**, 194503 (2004).
- ²⁹F. Rincon, "Anisotropy, inhomogeneity and inertial-range scalings in turbulent convection," *J. Fluid Mech.* **563**, 43 (2006).
- ³⁰J. Schumacher, "Lagrangian dispersion and heat transport in convective turbulence," *Phys. Rev. Lett.* **100**, 134502 (2008).
- ³¹F. Chillà and J. Schumacher, "New perspectives in turbulent Rayleigh-Bénard convection," *Eur. Phys. J. E* **35**, 58 (2012).
- ³²A. Brandenburg, "Stellar mixing length theory with entropy rain," *Astrophys. J.* **832**, 6 (2017).
- ³³P. J. Käpylä, M. Rheinhardt, A. Brandenburg, R. Arlt, M. J. Käpylä, A. Lagg, N. Olsper, and J. Warnecke, "Extended subadiabatic layer in simulations of over-shooting convection," *Astrophys. J. Lett.* **845**, L23 (2017).
- ³⁴P. J. Käpylä, "Overshooting in simulations of compressible convection," *Astron. Astrophys.* **631**, A122 (2019).
- ³⁵J. Schumacher and K. R. Sreenivasan, "Colloquium: Unusual dynamics of convection in the Sun," *Rev. Mod. Phys.* **92**, 041001 (2020).
- ³⁶A. Pandey, J. Schumacher, and K. R. Sreenivasan, "Non-Boussinesq low-Prandtl-number convection with a temperature-dependent thermal diffusivity," *Astrophys. J.* **907**, 56 (2021).
- ³⁷J. C. Kaimal and J. J. Fennigan, *Atmospheric Boundary Layer Flows* (Oxford University Press, New York, 1994).
- ³⁸D. Etling and R. A. Brown, "Roll vortices in the planetary boundary layer: A review," *Boundary-Layer Meteorol.* **65**, 215 (1993).
- ³⁹B. W. Atkinson and J. W. Zhang, "Mesoscale shallow convection in the atmosphere," *Rev. Geophys.* **34**, 403, <https://doi.org/10.1029/96RG02623> (1996).
- ⁴⁰S. S. Zilitinkevich, A. Grachev, J. C. R. Hunt *et al.*, "Surface frictional processes and non-local heat/mass transfer in the shear-free convective boundary layer," in *Buoyant Convection in Geophysical Flows*, edited by E. J. Plate (Springer, 1998), pp. 83–113.
- ⁴¹G. S. Young, D. A. R. Kristovich, M. R. Hjelmfelt, and R. C. Foster, "Rolls, streets, waves and more," *Bull. Am. Meteorol. Soc.* **83**, 997–1002 (2002).
- ⁴²T. Elperin, N. Kleeorin, I. Rogachevskii, and S. S. Zilitinkevich, "Formation of large-scale semi-organized structures in turbulent convection," *Phys. Rev. E* **66**, 066305 (2002).
- ⁴³T. Elperin, N. Kleeorin, I. Rogachevskii, and S. S. Zilitinkevich, "Tangling turbulence and semi-organized structures in convective boundary layers," *Boundary-Layer Meteorol.* **119**, 449–472 (2006).
- ⁴⁴T. Elperin, I. Golubev, N. Kleeorin, and I. Rogachevskii, "Large-scale instabilities in a nonrotating turbulent convection," *Phys. Fluids* **18**, 126601 (2006).
- ⁴⁵S. Chandrasekhar, *Hydrodynamic and Hydromagnetic Stability* (Oxford University Press, Oxford, 1961).
- ⁴⁶P. G. Drazin, *Introduction to Hydrodynamic Stability* (Cambridge University Press, Cambridge, 2002).
- ⁴⁷W. H. Reid and D. L. Harris, "Some further results on the Bénard problem," *Phys. Fluids* **1**, 102 (1958).
- ⁴⁸L. Barel, A. Eidelman, T. Elperin, G. Fleurov, N. Kleeorin, A. Levy, I. Rogachevskii, and O. Shildkrot, "Detection of standing internal gravity waves in experiments with convection over a wavy heated wall," *Phys. Fluids* **32**, 095105 (2020).
- ⁴⁹S. Toppaladoddi, S. Succi, and J. S. Wettlaufer, "Roughness as a route to the ultimate regime of thermal convection," *Phys. Rev. Lett.* **118**, 074503 (2017).
- ⁵⁰W. D. McComb, *The Physics of Fluid Turbulence* (Oxford Science Publ., Oxford, 1990).
- ⁵¹L. Ts. Adzhemyan, N. V. Antonov, and A. N. Vasil'ev, *The Field Theoretic Renormalization Group in Fully Developed Turbulence* (Gordon & Breach, London, 1999).
- ⁵²A. Yoshizawa, S.-I. Itoh, and K. Itoh, *Plasma and Fluid Turbulence: Theory and Modelling* (Institute of Physics, Bristol, 2003).
- ⁵³T. Elperin, N. Kleeorin, and I. Rogachevskii, "Isotropic and anisotropic spectra of passive scalar fluctuations in turbulent fluid flow," *Phys. Rev. E* **53**, 3431 (1996).
- ⁵⁴E. Jurčišinová and M. Jurčišin, "Diffusion in anisotropic fully developed turbulence: Turbulent Prandtl number," *Phys. Rev. E* **94**, 043102 (2016).
- ⁵⁵W. Kays, "Turbulent Prandtl number—Where are we?," *J. Heat Transfer* **116**, 284 (1994).
- ⁵⁶D. Li, "Turbulent Prandtl number in the atmospheric boundary layer—Where are we now?," *Atmos. Res.* **216**, 86 (2019).
- ⁵⁷D. Stretch, J. Rottman, S. Venayagamoorthy, K. K. Nomura, and C. R. Rehmann, "Mixing efficiency in decaying stably stratified turbulence," *Dyn. Atmos. Oceans* **49**, 25–36 (2010).
- ⁵⁸Y. Ohya, "Wind-tunnel study of atmospheric stable boundary layers over a rough surface," *Boundary-Layer Meteorol.* **98**, 57 (2001).
- ⁵⁹S. S. Zilitinkevich, T. Elperin, N. Kleeorin, and I. Rogachevskii, "Energy- and flux-budget (EFB) turbulence closure model for the stably stratified flows, Part I: Steady-state, homogeneous regimes," *Boundary-Layer Meteorol.* **125**, 167 (2007).
- ⁶⁰S. S. Zilitinkevich, T. Elperin, N. Kleeorin, I. Rogachevskii, and I. Esau, "A hierarchy of energy- and flux-budget (EFB) turbulence closure models for stably stratified geophysical flows," *Boundary-Layer Meteorol.* **146**, 341 (2013).
- ⁶¹N. Kleeorin, I. Rogachevskii, and S. Zilitinkevich, "Energy and flux budget closure theory for passive scalar in stably stratified turbulence," *Phys. Fluids* **33**, 076601 (2021).